Science Arts & Métiers (SAM)
is an open access repository that collects the work of Arts et Métiers Institute of Technology researchers and makes it freely available over the web where possible.

This is an author-deposited version published in: https://sam.ensam.eu
Handle ID: .http://hdl.handle.net/10985/23602

To cite this version :

Zimo WANG, Faissal CHEGDANI, Neehar YALAMARTI, Behrouz TAKABI, Bruce TAI, Mohamed EL MANSORI, Satish BUKKAPATNAM - Acoustic Emission Characterization of Natural Fiber Reinforced Plastic Composite Machining Using a Random Forest Machine Learning Model - Journal of Manufacturing Science and Engineering - Vol. 142, n°3, p.031003 - 2020

Any correspondence concerning this service should be sent to the repository Administrator : scienceouverte@ensam.eu

Zimo Wang[1]
Department of Industrial and Systems Engineering,
Texas A&M University,
College Station, TX 77843
e-mail: zimowang@tamu.edu

Faissal Chegdani
Arts et Métiers ParisTech,
MSMP Laboratory/EA7350,
Rue Saint Dominique BP508,
Châlons-en-Champagne 51006, France
e-mail: faissal.chegdani@ensam.eu

Neehar Yalamarti
Department of Industrial and Systems Engineering,
Texas A&M University,
College Station, TX 77843
e-mail: yneehar@tamu.edu

Behrouz Takabi
Department of Mechanical Engineering,
Texas A&M University,
College Station, TX 77843
e-mail: btakabi@tamu.edu

Bruce Tai
Department of Mechanical Engineering,
Texas A&M University,
College Station, TX 77843
e-mail: btai@tamu.edu

Mohamed El Mansori
Arts et Métiers ParisTech,
MSMP Laboratory/EA7350,
Rue Saint Dominique BP508,
Châlons-en-Champagne 51006, France
e-mail: mohamed.elmansori@ensam.eu

Satish Bukkapatnam
Department of Industrial and Systems Engineering,
Texas A&M University,
College Station, TX 77843
e-mail: satish@tamu.edu

Acoustic Emission Characterization of Natural Fiber Reinforced Plastic Composite Machining Using a Random Forest Machine Learning Model

Natural fiber reinforced plastic (NFRP) composites are eliciting an increased interest across industrial sectors, as they combine a high degree of biodegradability and recyclability with unique structural properties. These materials are machined to create components that meet the dimensional and surface finish tolerance specifications for various industrial applications. The heterogeneous structure of these materials—resulting from different fiber orientations and their complex multiscale structure—introduces a distinct set of material removal mechanisms that inherently vary over time. This structure has an adverse effect on the surface integrity of machined NFRPs. Therefore, a real-time monitoring approach is desirable for timely intervention for quality assurance. Acoustic emission (AE) sensors that capture the elastic waves generated from the plastic deformation and fracture mechanisms have potential to characterize these abrupt variations in the material removal mechanisms. However, the relationship connecting AE waveform patterns with these NFRP material removal mechanisms is not currently understood. This paper reports an experimental investigation into how the time–frequency patterns of AE signals connote the various cutting mechanisms under different cutting speeds and fiber orientations. Extensive orthogonal cutting experiments on unidirectional flax fiber NFRP samples with various fiber orientations were conducted. The experimental setup was instrumented with a multisensor data acquisition system for synchronous collection of AE and vibration signals during NFRP cutting. A random forest machine learning approach was employed to quantitatively relate the AE energy over specific frequency bands to machining conditions and hence the process microdynamics, specifically, the phenomena of fiber fracture and debonding that are peculiar to NFRP machining. Results from this experimental study suggest that the AE energy over these frequency bands can correctly predict the cutting conditions to ~95% accuracies, as well as the underlying material removal regimes.
[DOI: 10.1115/1.4045945]

Keywords: natural fiber reinforced composites, acoustic emission sensor, random forest, smart sensing and in-process monitoring

1 Introduction

Natural fiber reinforced plastic (NFRP) composites have recently received considerable interest in the industry [1–4]. Their high degree of biodegradability and recyclability offers tremendous economic and ecological advantages for sustainable manufacturing. Machining of NFRPs is an essential operation for finishing industrial products from such composite materials. In fact, the viability of fiber-reinforced plastics for various industrial applications is largely determined by the machined surface quality [5]. The texture and the finish of the machined surfaces of fiber-reinforced composites have a fundamental bearing on the mechanical properties (strength and hardness) and the geometric tolerance [6,7].

While significant investigations of the mechanics of material removal in fiber-reinforced composites have been reported, relatively fewer attempts have been made to characterize the machining of NFRP composites [8]. The machining process for fiber-reinforced composites involves complicated material removal mechanisms [9] that include a combination of shear deformation of the matrix material, fractures across the natural fibers, fiber pull-out, fiber–matrix detachment through tensile fracture, shearing and sliding along the fiber orientation directions, and delamination of fiber bundles [9–11]. Earlier investigations suggest that the cutting mechanisms may highly depend on fiber orientation angle (FOA) and matrix properties [12]. Machining of NFRP is further complicated by the multiscale nature of the fibers themselves [2], as well as the prevalence of significant thermal effects [1].

For example, Fig. 1 shows the machined surface of an NFRP composite with a rough texture resulting from the presence of fiber protrusions spread over the surface even when the machining process was well controlled. These protrusions result whenever natural fibers are cut and/or pulled out across and along their lay direction. As most natural fibers are highly flexible and heterogeneous over multiple geometric scales (e.g., the material composition

[1]Corresponding author.

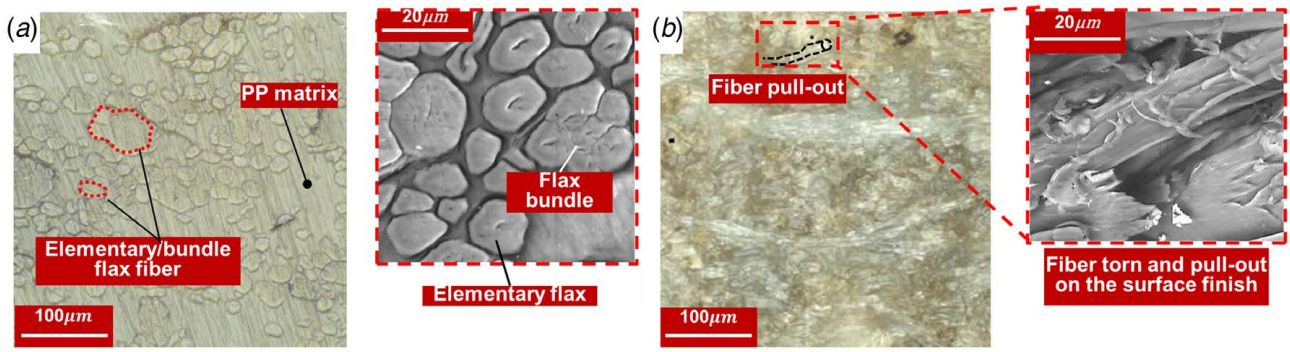

Fig. 1 **(*a*) Surface obtained from polishing a flax fiber-reinforced plastic material showing a clear contour of flax fibers and basin PP matrix (with a magnified SEM image for showing the elementary fiber and the fiber bundle) and (*b*) surface finished using orthogonal cutting processes in which the torn/broken-off fibers are randomly oriented on the surface finish (with the SEM image showing detailed torn fibers on the finished surface)**

and mechanical properties vary greatly from macro- to micro- to nano-scales [2]), the defects on machined surfaces affect the integrity of the finished surface and consequently reduce mechanical properties and geometric and dimensional tolerances, hence impeding the emerging industrial applications of NFRP composites.

Currently, investigations into the machining of NFRP composites rely heavily on offline approaches that employ mechanical property testing and alternative imaging and microscopy instruments to characterize the strength, thermomechanics, surface morphology, and chip formation [13]. While these methods have shed significant light on various modes of material removal and surface modification [14,15], they cannot fully capture the effects of the enormous statistical heterogeneity and variations in distributions of fibers over multiple scales of the matrix on the material removal mechanisms. In addition, these offline characterization tools are often unwieldy for real-time monitoring of the NFRP machining processes, and a sensor-based in-process monitoring approach is desirable to observe and delineate the diverse material removal mechanisms prevalent during NFRP cutting, to characterize the cutting process in real time, and to provide real-time predictions of the machined surface quality for timely intervention for quality assurance [12,16,17].

Conventional sensor technologies may have a limited signal-to-noise ratio (SNR) and are often insensitive to the subtle variations in cutting processes at high precision levels, where the cutting dimensions are of the order of a few micrometers and cutting force values are smaller than those in conventional machining processes [18]. Acoustic emission (AE), which emanates from the deformation, fracture, and/or friction mechanisms at the various tool, workpiece, and chip interfaces of machining, can be sensitive to monitor and enable us to discern among the various material removal mechanisms in NFRP machining. AE can also provide information related to chip entanglement, crack formation and propagation, and chip breakage in this process [19,20]. As detailed in Section 2, very little, if any, work has been done to study AE monitoring of the NFRP machining process.

2 Background

Earlier applications of AE for characterizing traditional glass and carbon fiber-reinforced polymer composites employed approaches developed in the nondestructive testing literature for measuring and localizing the damage [21–23]. For machining applications, however, environmental noise/inference needs to be maintained at a level that ensures an adequate signal-to-noise (SNR) ratio. Many of the underlying dynamics of machining processes are complicated, and the signals are often contaminated with a high level of environmental noise. Consequently, how to analyze the nature of the nonstationary AE signals during NFRP machining remains a major challenge.

Initial investigations of AE in machining have focused mostly on relating various statistical quantifiers of the signal patterns to predict machining conditions [24,25]. One of the earlier research thrusts was based on applying advanced machine learning approaches to estimate the machining process state using extracted frequency features of AE signals. Kamarthi et al. [26] and Pittner et al. [27,28] presented a neural network that extracted features using the wavelet decomposition on a multisensor setup for detecting tool wear. The microdynamics of the AE signal have also been investigated by Bukkapatnam et al. [29], and a recurrent neural network framework that uses the fractal properties of the attractor of the underlying dynamic system along with other machining parameters as the training inputs was developed to predict flank wear in machining. Furthermore, Rao et al. [30] applied a recurrent predictor neural network to capture the complex nonlinear and nonstationary evolution of the process underlying the measured vibration and AE signals and detect the incipient surface deterioration in ultraprecision machining processes. Cheng et al. [31] applied the Gaussian process with extracted statistical features as well as features based on the nonlinear recurrent analysis for online prediction of the surface morphology. Some statistical analysis approaches [25,32] have been presented to analyze the AE for monitoring of the cutting tool condition and to relate the AE signal features to the metal cutting process parameters. Lee et al. [18] discussed the unique requirements for monitoring precision manufacturing processes and the suitability of AE as a monitoring technique at the precision scale. A statistical modeling approach from our earlier effort [33] was aimed at handling transient behaviors during ultraprecision machining processes. However, most of these approaches may rely heavily on data-driven modeling and consequently lack explanations for the physical principles connecting the acoustic emission signal to the process microdynamics. Chang and Bukkapatnam [34,35] addressed the connection between AE sensor signal waveforms and the microdynamics for machining ductile metals. The model that represents the propagation of AE waveform signals from the plastic deformation in the shear zone suggests that AE energy is highly related to the shear strain and the shear strain rate.

Investigations into the characteristics of AE waveforms from NFRP composite machining, especially those attempting to understand the relationships connecting the measured AE signals and the NRFP machining microdynamics, have received very little attention. This lack of attention is mostly due to the difficulties of characterizing the complicated material removal mechanisms that govern NFRP composite machining. Some research efforts have also investigated the spectral characteristics AE during the machining processes of polymer matrix composite materials [36,37]. These investigations suggest that AE frequency components are highly related to flank wear and workpiece surface modifications.

The present work investigates the AE characteristics related to the machining processes of NFRP composites using a data-driven

analytic approach that not only allows real-time sensing and detection of the variations in the microstructure of NFRPs during machining processes but also provides analytic insights toward explaining the deformation mechanism during machining of such NFRP materials. An experimental study is presented to relate AE signals from NFRP machining to the process conditions and the underlying material removal mechanisms. The experiments were conducted on an orthogonal cutting testbed equipped with a multisensor data acquisition system. To connect the AE signal patterns to the machining mechanisms of NFRP cutting, we employ a random forest machine learning model. This model aims to capture the underlying nonlinear relationship between predictors from AE signals and the estimate of the process condition without sustaining significant overfitting issues. The model was also employed subsequently to enable us to the spectral components of AE signals that are highly sensitive to various material removal mechanisms during the cutting of NFRPs. The remainder of this paper is organized as follows: the experimental setup and the framework of the present approach is presented in Sec. 3; Sec. 4 presents the results of the random forest modeling study and provides insights into the physical origins of the signal components; and Sec. 5 concludes the paper.

3 Experimental and Analysis Approach

3.1 Experimental Setup and Procedure. The experiments were conducted on an orthogonal cutting testbed as shown in the schematic diagram in Fig. 2. The setup consists of two linear sliders and a workpiece holder/clamping vice. The cutting tool setup was attached to one linear actuator (L70, Moog Animatics, Milpitas, CA) through a customized tool holder. A high-torque servomotor drives the linear actuator to ensure a consistent cutting speed. Mainly two types of sensors were mounted on the machine setup: two accelerometers (Kistler Type 8728A500) were mounted on the tool holder and the workpiece holder separately for gathering vibration signals, while an acoustic emission sensor (Physical Acoustics S9225) was mounted on the cutting tool holder for collecting acoustic emission signals during the orthogonal cutting processes. This sensor monitoring system was equipped with a data acquisition system (National Instrument compactDAQ with DAQ module NI-9223) that allows real-time data collection at a 1 MHz sampling rate for each sensor signal. Unidirectional flax fiber-reinforced polypropylene composites (UDF/PP) mounted on the clamp-on vice were used as workpiece samples to investigate the effect of the fiber orientation angle on the cutting process. The UDF/PP samples shown in Fig. 2(*c*) are manufactured by the material supplier *Composites Evolution—UK*. Each UDF/PP workpiece is a rectangular slab with dimensions of $20 \times 15 \times 4$ mm^3. The fiber volume fraction is 40%, and the fiber unidirectionality is maintained by polyester weft fiber with low-volume fraction (around 5%). The orthogonal cutting experiments were conducted with the depth of cut around 100 μm in different cutting conditions with varying cutting speeds ($v = 2$, 4, 6, 8, 10, and 12 m/min) and different FOAs (FOA = 0 deg, 45 deg, and 90 deg) relative to the cutting direction (shown in Fig. 2(*d*)). Polycrystalline diamond (PCD) cutting tool inserts (Sandvik Coromant- Model TCMW16T304FLP-CD10) with a tungsten carbide substrate (as shown in Fig. 2(*c*)) were employed for the experiments.

As noted earlier, the purpose of this study is to assess the ability of AE signals to discern various process conditions including changes in the cutting speed and orientation in real time. The ability to discern changes in the process parameters is essential (but not sufficient) for a sensor to be qualified for real-time monitoring applications. This ability is also important in NFRP machining because of the high levels of variation expected in the fiber orientation related to the cutting direction as well as in the speeds during the machining of complex geometries and profiles. Consistent with this notion, the present approach aims to estimate process conditions based on analyzing the spectral characteristics of AE signals gathered from orthogonal cutting experiments using a random forest model, as summarized in Fig. 3. We employed a total of 18 different experimental settings, each formed by a combination of six cutting speeds, $v = 2$, 4, 6, 8, 10, 12 m/min, and three FOAs, 0 deg, 45 deg, and 90 deg. Experiments were replicated three times at each combination. At the beginning of each experiment, the surface of each NFRPs sample was polished using sand paper with a grit size of $\sim 15\ \mu$m to ensure a consistent initial condition (i.e., smooth surface with minimal deformed protrusions). As the surface was machined, the data acquisition system recorded signals from three channels, *viz.,* two from the vibration sensors and one from an

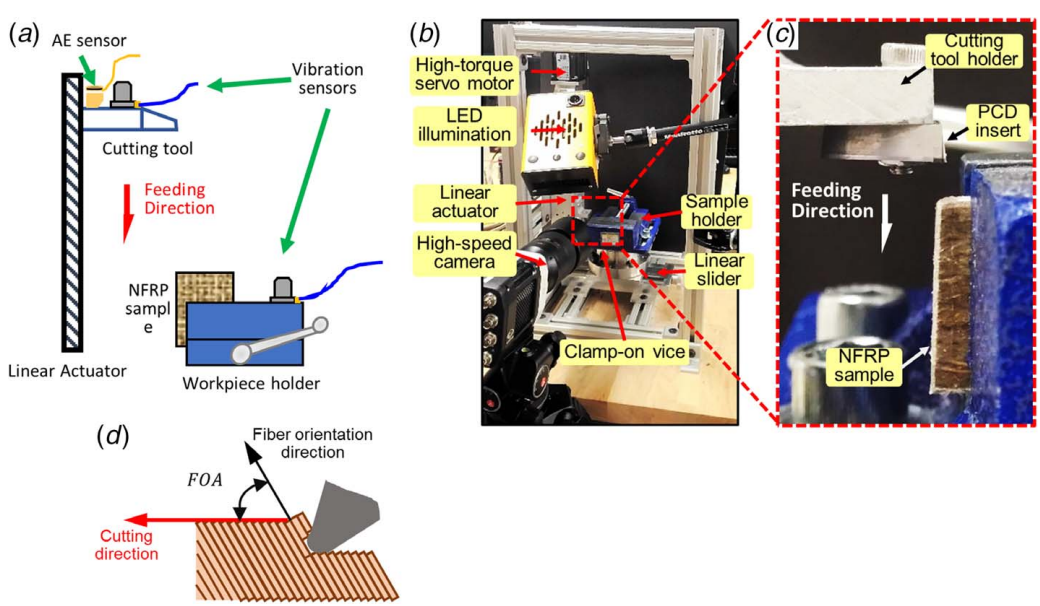

Fig. 2 Experimental setup for the orthogonal cutting process: (*a*) schematic diagram showing the mounting locations of AE and vibration sensors, (*b*) the orthogonal cutting machine setup with the installed high-speed camera and illumination system, (*c*) a PCD inserted cutting tool is held against the unidirectional flax fiber/PP matrix sample before the cutting begins, and (*d*) a schematic diagram showing the disposition of the cutting direction relative to the fiber orientation angle

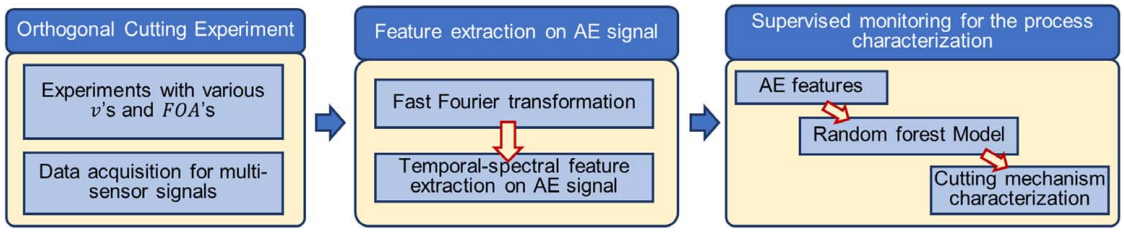

Fig. 3 A schematic diagram of the present research approach

AE sensor, at a sampling rate of 1 MHz. A moving windowed time–frequency analysis was performed to extract frequency features over the specified 125-μs long time windows. To investigate the relationship between the frequency responses of the AE signal and the fundamental cutting mechanisms during the cutting of the NFRPs, we treated the generated time–frequency features as inputs to a random forest model for characterizing the cutting processes with different fiber microstructures. Given the spectral features extracted from the online data during the machining, the trained random forest model was expected to predict the machining conditions, specifically the cutting speed and the FOA in real time. The details of this approach are presented in Secs. 3.2 and 3.3.

3.2 Time–Frequency Analysis and Feature Extraction. Figure 4 shows the representative sensor signals collected synchronously from the AE sensor and the two accelerometers mounted on the tool holder and the workpiece holder, respectively, during one cutting phase. The tool-approaching and the cutting phases are appropriately marked. As the cutting begins, we observe a sudden increase in the amplitude of Accelerometer 2 (attached to the workpiece holder). This increase allows us to isolate the dynamics of the cutting and the noncutting stages, such as tool-approaching and various cutting phases, by distinct changes in the variance of the vibration signal at the onset of cutting.

The AE signal captures the transients, i.e., time-varying frequency patterns associated with the material deformation and/or fractures that occur at irregular intervals during machining [38]. Hence, a time–frequency analysis is needed to generate the spectral features of the transient AE signal. Such temporal–spectral features are visually represented using a spectrogram as shown in Fig. 5(*a*), where the x-axis represents the time index and the y-axis is the frequency range. The energy of various frequency bands is represented using a color map. Such a spectrogram records the frequency components of the signal and their variations over time. The procedures for generating the temporal–spectral features can be summarized as follows:

(1) A sliding window with window width $L = 125$ is applied to collect a set of AE signals at time index t, i.e., $\{x_{t-L+1}, x_{t-L+2}, \ldots, x_t\}$.
(2) Then, the fast Fourier transformation (FFT) is applied to compute the frequency component:

$$X_k^{(t)} = \sum_{n=t-L+1}^{t} x_n e^{-\frac{i2\pi kn}{L}}, \quad k = 0, 1, \ldots, L-1 \tag{1}$$

where $\{x_n\}$ (for $n = t-L+1, t-L+2, \ldots, t$) is the time series of the AE signal within sliding window L, and the fast Fourier transformation generates the frequency components $\boldsymbol{X}^{(t)} = [X_1^{(t)}, X_2^{(t)}, \ldots, X_L^{(t)}]^{\mathrm{T}}$. After sequentially generating the frequency component vectors, $\boldsymbol{X}^{(t)}$'s (for $t = L, L+1, L+2, \ldots, T$), the matrix of the spectrogram can be represented as $M_{TF} = [\boldsymbol{X}^{(L)}, \boldsymbol{X}^{(L+\vartheta)}, \boldsymbol{X}^{(L+2\vartheta)}, \ldots, \boldsymbol{X}^{(T)}]$, where ϑ denotes the step of the sliding window. Essentially, the spectral energy over the high-frequency components of AE waveforms is related to the underlying microdynamics of the machining processes. The statistical analysis based on a Gini index [39], as presented in the sequel, suggests that these energy values can serve as important features to discern between various pairs of cutting conditions.

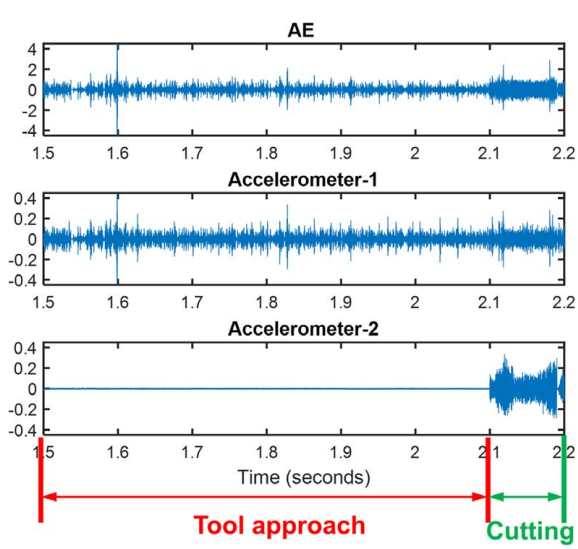

Fig. 4 Time portraits showing the synchronously gathered AE signal along with vibration signals from the tool holder (Accelerometer 1) and the workpiece holder (Accelerometer 2) during an orthogonal cutting process experiment ($v = 8$ m/min, FOA as 45 deg)

Apart from the spectral energy distribution via the time–frequency analysis, we had considered a few advanced signal analysis approaches, such as wavelet decomposition [40], Hilbert–Huang transformation (HHT)/empirical mode decomposition (EMD), and intrinsic time-scale decomposition (ITD). However, these methods have specific drawbacks in terms of being able to capture the energies across various bands. For example, as for wavelet decomposition, it has low resolution on high-frequency components, especially those that capture variations in the process microdynamics. A wavelet packet representation could provide fine resolution within specific frequency ranges [41]. However, most of the wavelet packet bases (especially, if the orthogonality condition is imposed) have an infinite support at time and/or frequency domain (i.e., every coefficient is estimated by taking all the samples of the AE signals). This complicates the extraction of the energies over various bands. For the HHT/EMD and ITD [42], it is not straightforward to extract frequency components from the intrinsic mode functions (IMFs). These representations introduce severe edge effects when decomposing the AE signals over multiple levels of IMFs, which amounts to losing the data points in the time domain.

Figures 6(*a*)–6(*c*) show the spectrograms of the AE and the two vibration signals, respectively, capturing the temporal–spectral features of the tool-approaching and the cutting phases. The spectrograms shown in Fig. 5 were generated by the FFT with a sliding window of 0.125 ms and a 50% time step (i.e., $\vartheta = 0.5L$), which

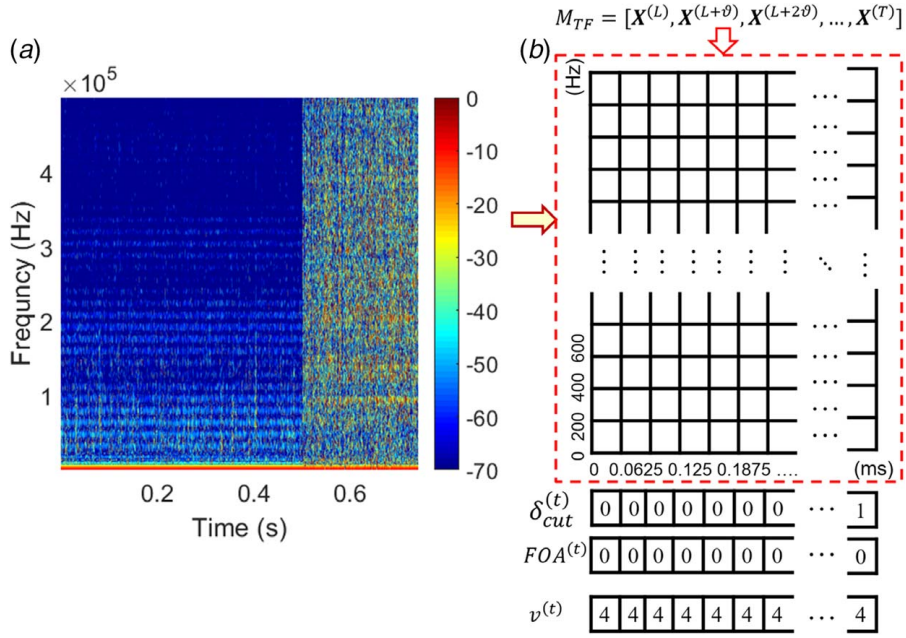

Fig. 5 A schematic diagram showing the temporal–spectral feature extraction with time stamp resolution of 0.125 ms, a 0.6725 ms overlap, and the frequency resolution as 200 Hz. The process responses $Y^{(t)} = [\delta_{cut}^{(t)}, \mathrm{FOA}^{(t)}, v^{(t)}]^{\mathrm{T}}$, where FOA = 0 deg and v = 4 m/min. Note that the matrix M_{TF} records the magnitudes of the Fourier components (as Volts) and their logarithmic amplitudes (in decibels) are depicted in the spectrogram to visually signify the frequency components' variations.

translates to a temporal resolution of 0.125 ms (x-axis), and we select 200 Hz as the spectral resolution (y-axis). Our choice of the window length and the overlap is based on the following rationale. AE sensor signals are composed of multiple AE pulses released from various events, such as fracture and dislocation avalanche that occur at frequency ranges of over 200 kHz (i.e., these events last just for a fraction of a microsecond up to a few microseconds (see Fig. 10)). We selected a 0.125-ms long time window, which is of sufficient length to achieve the frequency resolution to discern changes in the spectral shape and at the same time, not too long to ignore time variations of AE events (i.e., the transients). Similarly, a 50% was chosen to extract sufficient number of features and at the same time avoiding significant correlation (more specifically, multiple collinearity) among the features to train the random forest model. Taken together, the window length and the overlap allow us to effectively extract the salient time and frequency characteristics of the measured AE signals. The edge effect due to the sliding window may be ignored as the window size (0.125 ms duration) is smaller than durations of the overall recordings (which normally last for seconds) by 4–5 orders of magnitude. The dimensions of temporal–spectral features are illustrated in Fig. 5. The energy of each element in the spectrogram matrix is represented in a color map, ranging from −70 dB (blue colored) to 0 dB (red colored). The sensitivity of the AE sensor can be validated by the high-frequency response of the AE signal (Fig. 6(*a*)) compared with the vibration signals shown in Figs. 6(*b*) and 6(*c*). In fact, only the spectrogram of the AE signals showed remarkable/noticeable differences in the high-frequency ranges (>100 kHz).

Note that the multisensor setup allows a partition of the time–frequency features into cutting versus noncutting. Let τ_1 and τ_2 be the start and the end time stamps, respectively, of the segment for the cutting phase (e.g., the start and the end points of the red frame shown in Fig. 6(*a*)). Here, we denote the

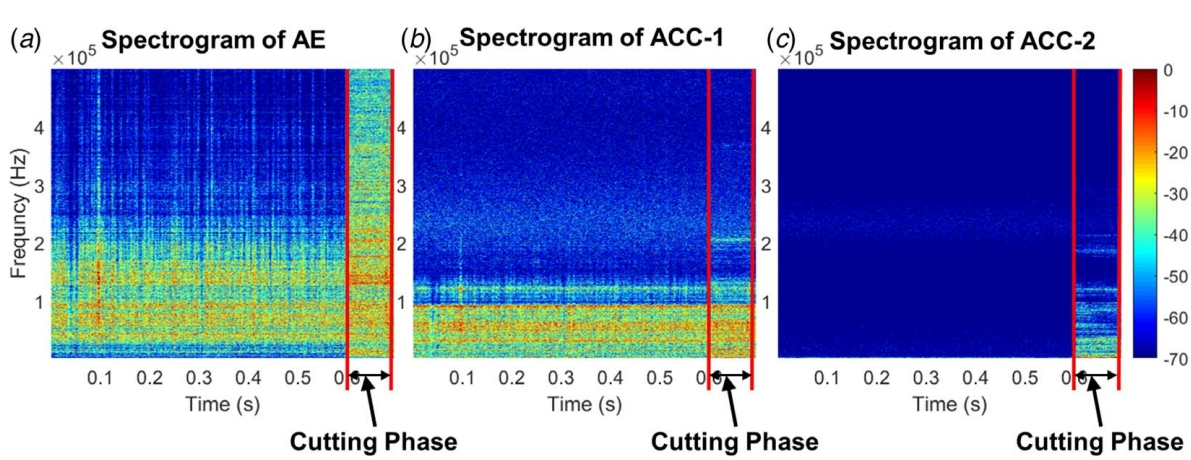

Fig. 6 The representative time–frequency domain spectrograms (in dB) gathered during an orthogonal cutting experiment (v = 8 m/min, FOA as 45 deg): (*a*) the AE sensor, (*b*) the Accelerometer-1, and (c) the Accelerometer-2. Here, the rectangular (red) frame at the right side of every plot indicates the temporal–spectral information during the cutting phase.

cutting phase partition using a series of indicators $\{\delta_{cut}^{(t)}\} = \{\delta_{cut}^{(L)}, \delta_{cut}^{(L+\vartheta)}, \delta_{cut}^{(L+2\vartheta)}, \ldots, \delta_{cut}^{(T)}\}$, where $\delta_{cut}^{(t)} = 1$ for $t \in [\tau_1, \tau_2]$ and $\delta_{cut}^{(t)} = 0$ otherwise. The response vector $\boldsymbol{Y}$ combines the cutting indicator with other control parameters for the experiments, i.e., $\boldsymbol{Y}^{(t)} = [\delta_{cut}^{(t)}, FOA^{(t)}, \quad v^{(t)}]^{\mathrm{T}}$ for $t = L, L+\vartheta, L+2\vartheta \ldots, T$, where T is the total length of the acquired data, FOA $\in \{0\text{ deg}, 45\text{ deg}, 90\text{ deg}\}$, and cutting speed $v \in \{2, 4, 6, 8, 10, 12\}$ (units in m/min). Given the time duration T_0 (in seconds) of the recording, here $T = T_0 \times Fs$, where Fs is the sampling rate ($Fs = 1$ MHz for all experiment recordings). Then, the extracted features, $\boldsymbol{X}$'s, as well as the process responses, $\boldsymbol{Y}$'s, for a single recording Ω can be represented in the following equation:

$$\Omega = [\boldsymbol{X}^{(t)\mathrm{T}}, \boldsymbol{Y}^{(t)\mathrm{T}}]^{\mathrm{T}} = \begin{bmatrix} \boldsymbol{X}^{(L)} & \boldsymbol{X}^{(L+\vartheta)} & \boldsymbol{X}^{(L+2\vartheta)} & \ldots & \boldsymbol{X}^{(T)} \\ \boldsymbol{Y}^{(L)} & \boldsymbol{Y}^{(L+2\vartheta)} & \boldsymbol{Y}^{(L+2\vartheta)} & \ldots & \boldsymbol{Y}^{(T)} \end{bmatrix} \quad (2)$$

3.3 Random Forest Classifier for Process Condition Monitoring. The random forest approach [43] is applied to capture empirical relationships between the AE spectral features $\{\boldsymbol{X}^{(t)}\}$ and $\{y^{(t)}\}$, where $y^{(t)}$ is a subset of response $\{\boldsymbol{Y}^{(t)}\}$ (e.g., $y^{(t)} = \delta_{cut}^{(t)}$ for characterizing cutting versus noncutting phases and $y^{(t)} = \mathrm{FOA}^{(t)}$ for classifying the fiber orientation). During the training phase, the random forest approach (in Fig. 7) employs samples obtained, with replacement, from the training set $\{\boldsymbol{X}^{(t)}\}$ and $\{y^{(t)}\}$ to build multiple tree learning models. The decision rule for each tree learning model was based on the randomly selected features $\{\boldsymbol{X}^{(t)}\}$ [44,45]. Unlike conventional regression approaches [46], a random sampling and selection scheme allows a classification model to capture underlying nonlinear relationships without imposing biased structures or overfitting issues. The detailed procedures on training the random forest models are stated as follows [47].

Given a training dataset $\Omega' = \{(\boldsymbol{X}^{(L)\mathrm{T}}, y^{(L)\mathrm{T}}), (\boldsymbol{X}^{(L+\vartheta)\mathrm{T}}, y^{(L+\vartheta)\mathrm{T}}), \ldots, (\boldsymbol{X}^{(T)\mathrm{T}}, y^{(T)\mathrm{T}})\}$ ($y^{(t)} = \mathrm{FOA}^{(t)}$ for fiber orientation classification and $y^{(t)} = \delta_{cut}^{(t)}$ for the cutting versus noncutting phase), the random forest first generates B new training datasets Ω_i (for $i = 1, \ldots, B$), which have the same sample size as the original Ω', with some samples replaced in the dataset (also called bootstrap sampling). Consequently, some observations may be repeated in the new dataset Ω_i.

For each bootstrapped sample, the decision tree is constructed by the following procedures: at each node of the tree model, m features are randomly sampled and the best split among these randomly selected predictors is chosen (also called a feature bagging scheme). The splitting criterion at the node is chosen to minimize the sum of the squares, which allows the partition of m predictors into M regions $R_1, R_2, \ldots, R_M$. Assume that the splitting variable X_j is split at point x_j to segment the half plane as R_1 and R_2, where $R_1(j, x_j) = \{\boldsymbol{X} | X_j \le x_j\}$ and $R_2(j, x_j) = \{\boldsymbol{X} | X_j > x_j\}$. The splitting variable X_j and the split point x_j should be the optimal solution to the following objective [47]:

$$\min_{j, x_j} \left[\min_{c_1} \sum_{X_k \in R_1(j, x_j)} (y_k - c_1)^2 + \min_{c_2} \sum_{X_k \in R_2(j, x_j)} (y_k - c_2)^2 \right] \quad (3)$$

where the constants c_1 and c_2 are the responses in region R_1 and R_2. Note that the overall expected output/response in each region can be formulated as $f(X) = \sum_{s=1}^{M} c_s I(X \in R_s)$. The optimal constant value, $\widehat{c_S}$, is the average of response $y^{(t)}$ in region R_s, i.e., $\widehat{c_S} = \text{average}\,(y^{(t)} | X^{(t)})$. Hence, the constants can be solved by $\widehat{c_1} = \text{average}\,(y^{(t)} | X^{(t)} \in R_1(j, x_j))$ and $\widehat{c_2} = \text{average}\,(y^{(t)} | X^{(t)} \in R_2(j, x_j))$. The splitting algorithm is stopped once a fully binary tree model of a certain number of levels (in the default setup, 8 levels) is built.

For our case study, the inputs of the feature space are from the extracted spectrogram $\{\boldsymbol{X}^{(t)}\}$, and the training outputs $\{y^{(t)}\}$ are selected from the responses $\{\boldsymbol{Y}^{(t)}\}$. For the parameter selection, we chose the number of trees as $B = 100$ and 25 variables to randomly sample candidates at each decision split for all the cases tested, which results in a minimal out-of-bag error.

The random forest generally performs an implicit feature selection by using a small subset of all variables $\{X_j\}$ for the classification problem. Such subsets are regarded as "strong variables" for superior performance in handling high-dimensional data/features. The associated Gini importance values are the measures that visualize the results from the implicit feature selection of the random forest model and are commonly used as the indicator(s) of the feature relevance to the classification results.

Let $p_\kappa = \mathbb{N}_\kappa / \mathbb{N}$ be the fraction of the $\mathbb{N}_\kappa$ samples from the class FOA $= \{0\text{ deg}, 45\text{ deg}, 90\text{ deg}\}$ or $\delta_{cut} = \{0, 1\}$ ($\kappa \in$ FOA or δ_{cut}) of the total $\mathbb{N}$ samples at node ξ. The Gini impurity $Gini(\xi)$ is calculated as follows:

$$Gini(\xi) = 1 - \sum_{\kappa} p_\kappa^2 \quad (4)$$

The decrement $\Delta Gini$ is caused by the splitting and sending of the samples to two subnodes ξ_ϖ and ξ_ς (with fractions with respect to two subnodes $p_\varpi = \mathbb{N}_\varpi / \mathbb{N}$ and $p_\varsigma = \mathbb{N}_\varsigma / \mathbb{N}$). Threshold x_j on variable X_j is defined as follows:

$$\Delta Gini(\xi) = Gini(\xi) - p_\varpi Gini(\xi_\varpi) - p_\varsigma Gini(\xi_\varsigma) \quad (5)$$

A search over all variables at node ξ and over all possible segmentation threshold obtains a pair $\{X_j, x_j\}$ that allows a maximal $\Delta Gini$ value. The decrease in Gini impurity is recorded for all node $\{\xi\}$'s for all trees B and accumulated for all variable X_j's as:

$$I_{Gini}(X_j) = \sum_B \sum_\xi \Delta Gini_{\{X_j\}}(\xi, B) \quad (6)$$

Intuitively, this Gini importance value I_{Gini} indicates how often a particular feature $X_k^{(t)}$ was selected for a split and how large its overall discriminative value was for the classification problem [39].

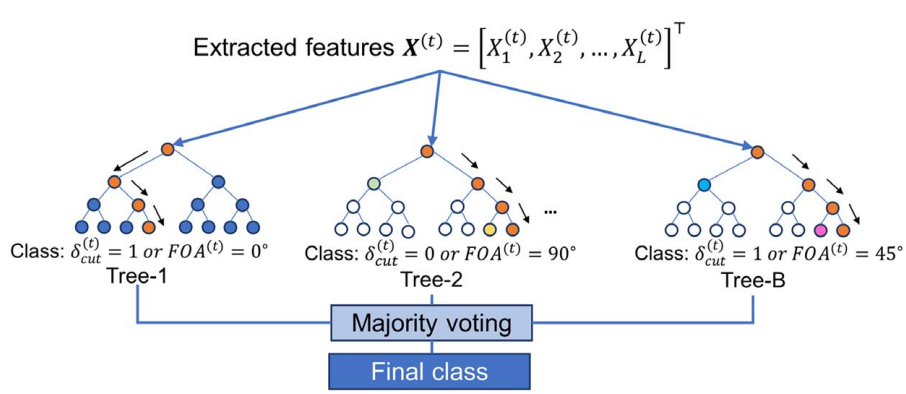

Fig. 7 The schematic diagram of the random forest machine learning approach

4 Acoustic Emission–Based Monitoring of the NFRP Machining Process

4.1 A Random Forest Model to Detect the Start and End of the Cutting Process Using Acoustic Emission Signals. Given the extracted AE time–frequency features $\{\boldsymbol{X}^{(t)}\}$ and the response $\{y^{(t)}\} = \{\delta_{cut}^{(t)}\}$, a random forest model was trained to discern between the cutting and the noncutting phases. Specifically, for both training and testing data sets, 20% of the data were gathered during the cutting operation and the other 80% data during the noncutting operation. The overall data set was split into five subgroups, and each subgroup was tested with the random forest classification. Each data set selected around 1400 samples for training and about 600 samples for testing. We compared the present approach with Fisher's linear discriminant analysis (LDA). At the outset, conventional LDA approaches are effective only when the signal features gathered from every pair of process conditions (e.g., cutting versus noncutting, and FOA) can be separated (in the feature space) using a linear boundary (as in a hyperplane). The LDA models also assume that feature values from different conditions can be grouped into distinct Gaussian clusters with equal variance and that they are well separated from each other. In contrast, a random forest can separate out the signal features from various conditions using complex nonlinear boundaries and does not make any assumptions on the clustering of the feature values. Table 1 summarizes the classification results (in terms of overall accuracy, true positive rate (TPR), and true negative rate (TNR)) from the presented approach versus LDA for the present case study. Here, the TPR measures the proportion of actual samples that are correctly identified as from the cutting condition, and TNR represents the percentage of the samples correctly classified as from the noncutting condition. It is evident that the average accuracy of the random forest model is ∼94%, which is 20% higher than that of LDA. In addition, TPR increases from 0.45 with LDA to 0.84 with the random forest model.

Table 1 Cross-validation comparisons of random forest versus LDA based for the study case of cutting versus noncutting

		Accuracy	True positive rate	True negative rate
Random forest	Mean	0.9427	0.8390	0.9819
	Std	0.0124	0.0455	0.0079
Fisher's LDA	Mean	0.7674	0.4443	0.8189
	Std	0.0264	0.0566	0.0340

The resulting Gini importance values from the classification problem of the cutting versus noncutting phases are shown in Fig. 8(*a*). Note that each y-axis label refers to the frequency (kHz) in the temporal–spectral matrix (e.g., the first Gini index relates to the frequency response in 358.4 kHz). A higher Gini importance value of a frequency range indicates a greater contribution of the spectral feature to improve the accuracy. Interestingly, the most significant frequency features determining the accuracy of the random forest based on Gini importance are in the frequency ranges of 350 kHz to 440 kHz. The spectrogram in Fig. 8(*b*) suggests that more energy is contained in such a frequency range (highlighted in the pink frame) during the cutting compared with the noncutting phase. However, conventional vibration sensors are not suited for monitoring processes at such high frequencies, as they do not have an adequate dynamic response in this range. This high-frequency response highlights the significance of using an AE sensor instead of the more commonly used vibration sensor for fast, high-frequency (>100 kHz) detection of subtle changes during machining at microscales.

4.2 Supervisory Monitoring for the Fiber Orientation Effect. In the next case study, we investigated the effect of fiber orientation on machining microdynamics and the corresponding AE characteristics. Given the extracted time–frequency features $\{\boldsymbol{X}^{(t)}\}$ and the response $\{y^{(t)}\} = \{\mathrm{FOA}^{(t)}\}$, a random forest model was trained to predict the fiber orientation based on the spectral features of AE. Here, spectral values above 100 kHz in every column of the AE spectrogram (Fig. 9) were used as the features because the high-frequency spectral components have the time resolution needed to detect changes in their incipient states. As shown in Fig. 9, the AE time portraits as well as the temporal–spectral features show significant differences between the fiber orientation with 90 deg and the others under the same cutting speed (4 m/min). In contrast, the signal variance between fiber orientations with 0 and 45 deg are less noticeable in the time domain compared with the difference between their temporal–spectral features plotted in the spectrograms in Fig. 9.

The results of classification accuracy are listed in Table 2 (results are generated based on five computations on the combined data from different cutting speeds). Here, in the confusion matrix, each row

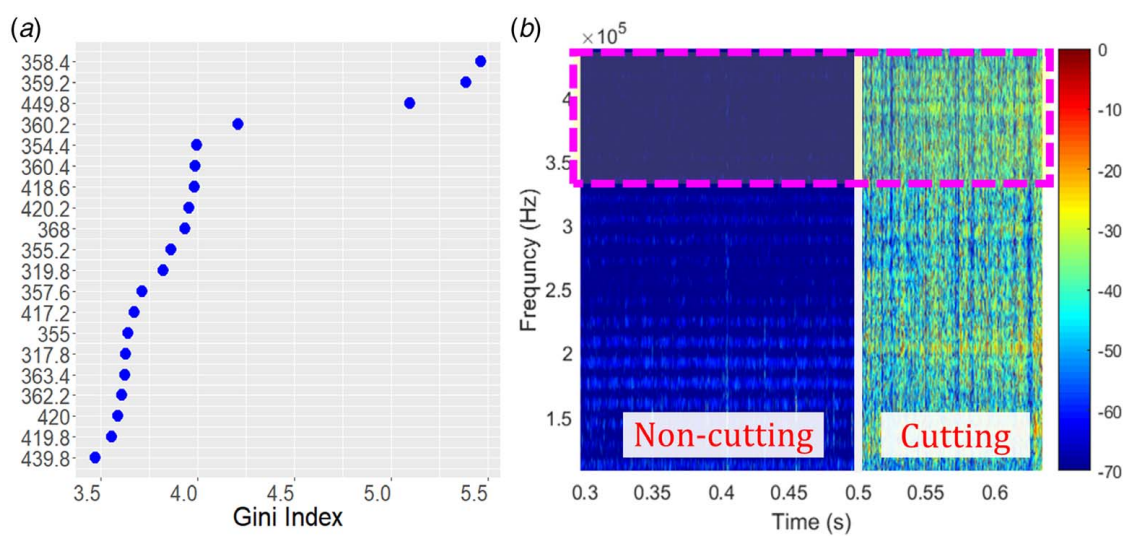

Fig. 8 Results for classifying cutting versus noncutting: (*a*) the Gini importance plot with the significant features labeled (y-axis) by the frequency band (kHz) (e.g., the highest Gini value corresponds to the frequency response at 358.4 kHz) and (*b*) a spectrogram representation of the noncutting phase versus the cutting phase (white line segmented) with corresponding significant frequency bands highlighted in the pink frame

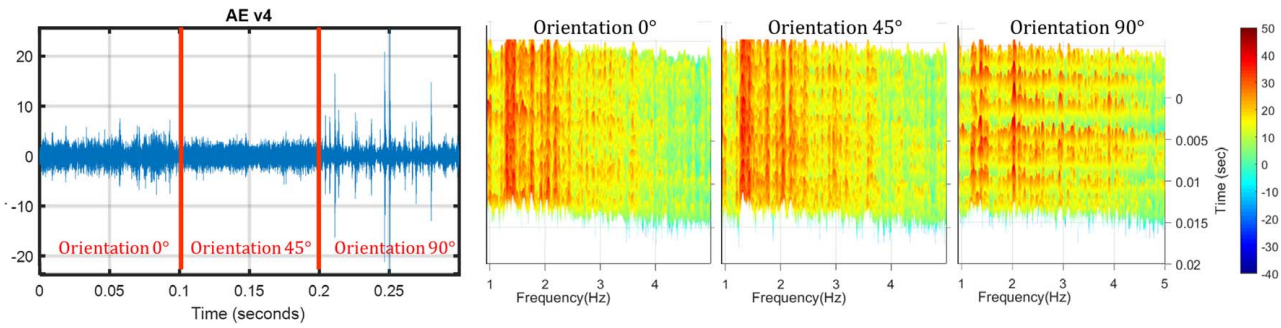

Fig. 9 The combined AE signals recorded during orthogonal cutting with different FOAs at the same cutting speed (4 m/min) and three spectrograms, one for each FOA

Table 2 Cross-validation results for various fiber orientations using the random forest

Confusion matrix		Predicted 0 deg	45 deg	90 deg
Actual	0 deg	0.8531	0.1259	0.0210
	45 deg	0.1354	0.7446	0.1200
	90 deg	0.2047	0.1913	0.6040

represents the actual class and the columns are the predicted results for three classes. The value inside each element $[\kappa_i, \kappa_j]$ of the confusion matrix represents the portion of samples from actual class κ_i that are identified as class $\kappa_j(\kappa_i, \kappa_j \in \text{FOA} = \{0\text{ deg}, 45\text{ deg}, 90\text{ deg}\})$. The results suggest a statistically significant difference between study cases with 0 deg of orientation and all others. This difference may be due to the cutting mechanisms of different fiber orientations. In the 0 deg study case, the fibers are mostly aligned along the cutting direction. Therefore, for such an orientation, the cutting process is predominantly with the PP matrix removal and with very few fibers sliding/shearing along interfacial areas during material removal. In contrast, the cutting mechanism in the 45- and 90-deg orientations involves more cutting and pulling of fibers. Even though the signal in the 90-deg orientation has significantly different time portraits, which exhibit strong transient behaviors, the random forest could recognize its difference compared with other groups with around 60% accuracy. This result may indicate that other factors affecting the cutting mechanism and/or the material removal (e.g., varying cutting speeds) are not considered in the random forest model.

Results from previous investigations [6,48–50] into the machinability of fiber-reinforced composites suggest that as the cutting speed increases, the surface integrity drops. This may be due to the viscoelastic property of the composite materials. Also, higher cutting speeds may increase the shear stress on the chip tool interface, which in turn increases the strain/elongation of the fibers nonlinearly. For all these reasons, more fiber failures may occur (fiber breakages, pull-out, and some inefficient shearing causing microfiber failures of the cellulose structure), along with more plastic deformation of the matrix per unit time for higher speed cutting conditions, resulting in more energy released. The evidence can be found in the time portraits of AE signals (see Fig. 10), which were recorded during two experiments with the same FOA but different cutting speeds. Here, the blue lines refer to the AE signal gathered under machining parameters $v = 12$ m/min and FOA = 90 deg, and the yellow-lined AE signal is from the experiment with $v = 2$ m/min and FOA = 90 deg. It may be noticed that even under the same fiber orientation angle, a higher cutting speed (12 m/min) may result in a larger AE envelope. That is, when analyzing the cutting mechanisms with respect to different fiber orientations, the cutting speed also needs to be considered.

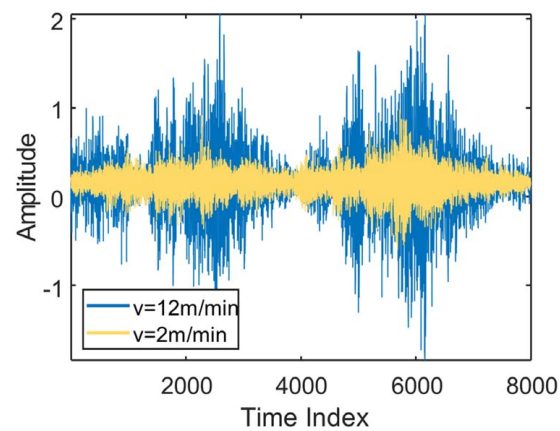

Fig. 10 Comparison of the waveforms of the AE signals between two cutting speeds: 2 m/min (yellow) versus 12 m/min (blue) for FOA = 90 deg

Clearly, the increase in the AE amplitude due to an increase in the cutting speed may be attributed to the increase in the material shear rates, and hence, sources of AE increase with an increase in the cutting speed.

The performance of the random forest model (in terms of classification accuracy) for identifying the correct FOA using AE signals collected at six different cutting speeds was compared with that of LDA (see Table 3). Three cases of different FOAs (0 deg versus 90 deg, 0 deg versus 45 deg, and 45 deg versus 90 deg) were investigated under each cutting speed. Compared with LDA, the random forest's accuracy for discerning fiber orientations increased by ~30% (from 65% to 94.8%). As noted earlier, such an improvement is a consequence of the random forest relaxing the strong assumption LDA makes on how features are clustered and distributed. Pertinently, the random forest employs an ensemble of decision trees, such that each tree is trained using a different,

Table 3 Accuracy of FOA classification for various fiber orientations under each cutting speed (m/min) (in comparisons with LDA)

	$v = 2$	$v = 4$	$v = 6$	$v = 8$	$v = 10$	$v = 12$
Random forest						
0 versus 45	0.9719	0.9583	0.9313	0.9396	1.0000	0.9031
0 versus 90	0.9594	0.9656	0.9563	0.9492	0.9281	0.8750
45 versus 90	0.9938	0.9792	0.9478	0.9271	0.9667	0.9031
LDA						
0 versus 45	0.7188	0.7125	0.6281	0.5688	0.7625	0.6219
0 versus 90	0.6469	0.7031	0.7656	0.6680	0.5688	0.5844
45 versus 90	0.6813	0.6901	0.5344	0.5625	0.6563	0.6875

random subset of the features at each split of the tree model (see Supplementary data on the ASME Digital Collection that includes detailed tree structure for constructing this random forest model). This avoids the correlation between selected features. Also, the random forest provides metrics that help with feature selection as well as interpretation of the classification results. Specifically, it generates the quantifiers, such as Gini Index, to statistically indicate the extent to which every feature contributes to the classification accuracy.

The Gini index values for three cases are listed in Figs. 11(*a*)–11(*c*); Figs. 11(*d*)–11(*f*) depict comparisons of the spectrograms corresponding to these three cases (0 deg versus 45 deg, 0 deg versus 90 deg, and 45 deg versus 90 deg), where the vertical red line in each figure segments two orientation conditions. Note that here the pink blocks highlight the most significant frequency features (with highest Gini index values) suggested by the results from the random forest classification. Early work [51,52] suggests that AE signals with a frequency response above 350 kHz during failure tests of fiber-reinforced composites are more related to fiber breakage. Our case clearly shows that the most significant spectral features that distinguish 0 deg from 45 deg and 90 deg are above 350 kHz. As in the power spectrums of both Figs. 11(*d*) and 11(*e*), more energy in high frequencies (above 350 kHz) is observed for FOA*s* = 45 deg and 90 deg compared to FOA = 0 deg. When we compare the cutting processes for 45 deg versus 90 deg, the differences in the frequency components are less discernible, but the random forest model is able to select significant frequency features (frequency bands 260 kHz–280 Hz and 220–240 kHz, as highlighted in Fig. 11(*f*)) to recognize different fiber orientations (45 deg versus 90 deg) for cutting NFRPs. Such different features in certain high-frequency bands suggest that different responses of the AE sensor may be related to different types of failure modes/cutting mechanisms.

4.3 Acoustic Emission Signatures and the Fracture Energy During NFRP Machining. Unlike the brittle failure mechanisms that occur when cutting synthetic fiber (e.g., carbon and glass fiber) reinforced composites with the thermoset polymer matrix, the NFRP sample with the thermoplastic polymer matrix possesses high flexibility and follows ductile deformation behavior when undergoing transverse shear stress during orthogonal cutting [9]. For FOA = 0 deg, the cutting process is dominated by the matrix deformation under the shearing zone with some amount of debonding of the fibers along the cutting direction (matrix-fiber shearing) with a few episodes of fiber pull-out and microfiber failures (see Fig. 12). At FOA = 45 deg and 90 deg, however, micro-failures across the fiber axis are prevalent due to the shearing and tensile forces. Also, for the process under FOA = 45 deg, the interfacial shearing along the fiber orientation causes debonding between the fiber and the PP matrix. Moreover, intermittent fracture is one mechanism under FOA = 90 deg that results in fiber tensile failure and/or pull-out toward the cutting direction with a sudden increase in the cutting force.

Figure 13 shows the schematic diagrams of the chip formation of NFRPs under different FOAs. It may be noticed that because of the different orientation of fibers, the microstructure (elementary/bundle fibers and matrix-fiber bounds) may undergo anisotropic stress/strain, resulting in distinct failure modes of NFRP components during the material removal process. Consequently, the internal failures of the composites may manifest as different modes (e.g., fiber breakage and fiber–matrix debonding). The fracture energy

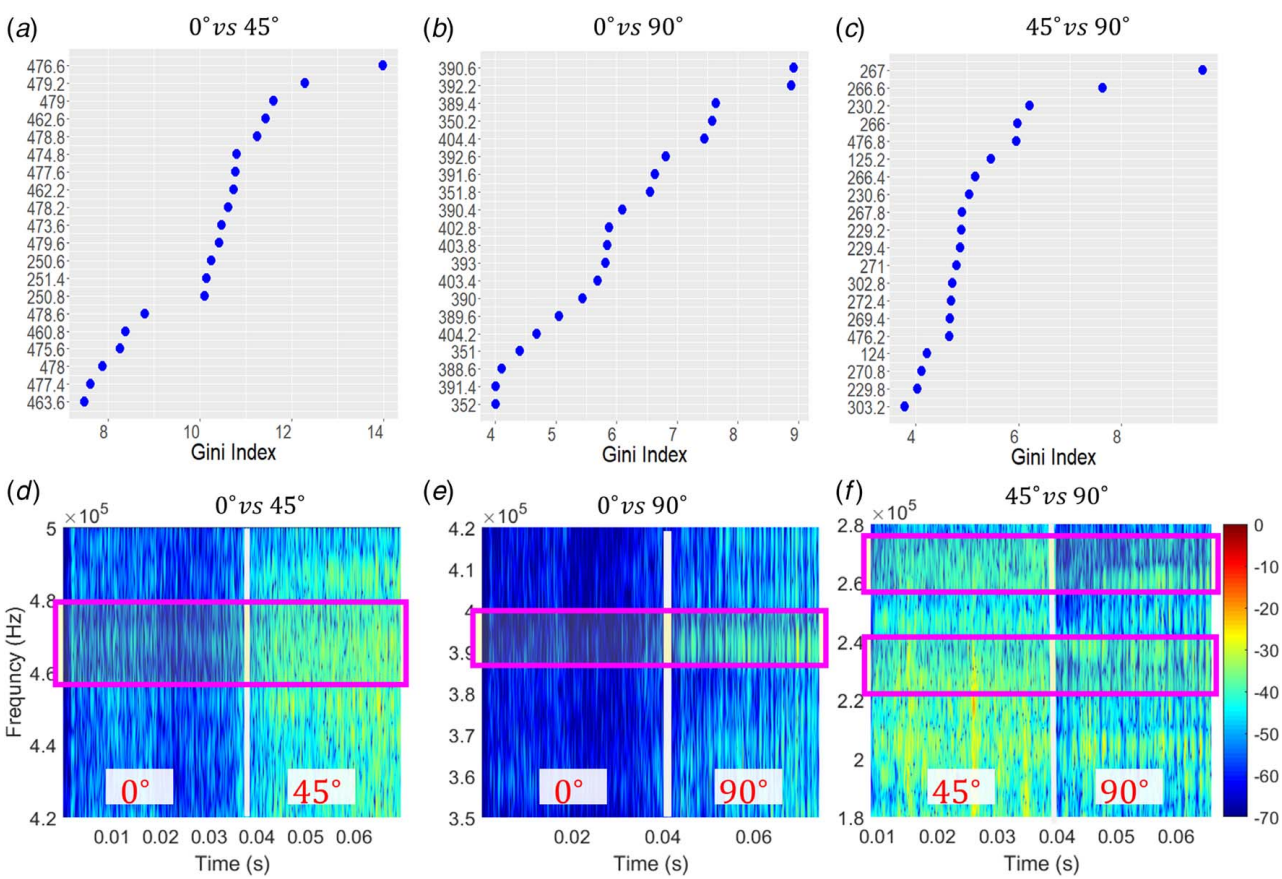

Fig. 11 GINI indices of the significant frequency components for three FOA classifiers: (*a*) 0 deg versus 45 deg, (*b*) 0 deg versus 90 deg, and (*c*) 45 deg versus 90 deg. The spectrograms of the juxtaposed AE signals show the differences in the frequency contents among these three cases: (*d*) 0 deg versus 45 deg, (*e*) 0 deg versus 90 deg, and (*f*) 45 deg versus 90 deg. The most significant frequency features are highlighted by pink frames.

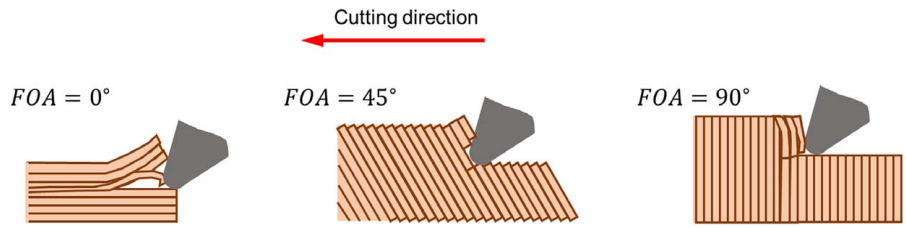

Fig. 12 A schematic diagram showing the cutting mechanisms under different fiber orientation angles [53]

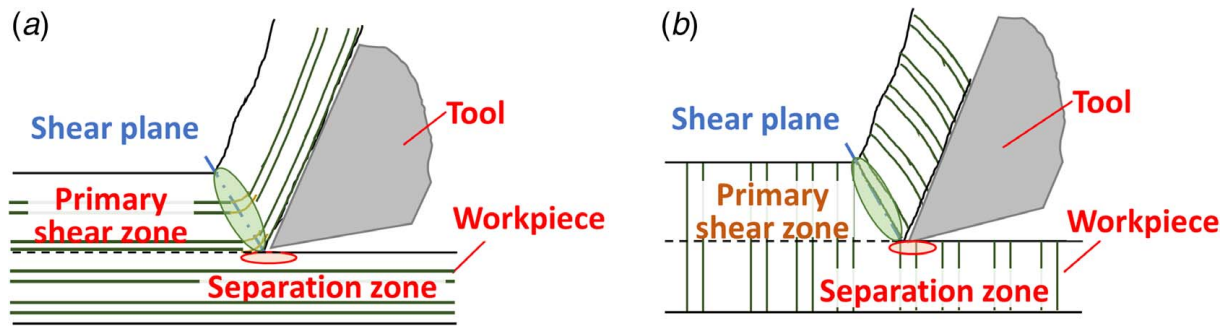

Fig. 13 The schematic diagrams showing the cutting modes and chip formation for different fiber orientation angles: (*a*) 0 deg and (*b*) 90 deg

released from such different failure modes may contribute to the generated AE waveform. The following fracture energy analysis of the cutting processes for NFRPs provides a theoretical explanation of the differences in the released fracture energy due to different microstructure variations and cutting speeds under each fiber orientation condition.

As for the orthogonal cutting processes only for thermoplastic composites such as the PP matrix in the tested NFRP samples, the power released during the shear stress can be formulated as follows:

$$E_S = \frac{F_S \cdot V_S}{b \cdot t_u \cdot V} = \frac{F_S}{b \cdot t_u} \cdot \frac{\cos\alpha}{\cos(\phi - \alpha)} \tag{7}$$

where V_S is the shearing speed, V is the cutting speed, b is the chip width, t_u is the uncut chip thickness (100 μm), and α is the rake angle. The shear angle ϕ is a function of the rake angle α and the friction angle β, i.e., $\phi = \pi/4 - \frac{1}{2}(\beta - \alpha)$. Then, the shear force F_S around the shearing zone can be formulated as [48] follows:

$$F_s = A_s \cdot \tau = \frac{t_u b}{\sin(\phi)} \cdot \tau \tag{8}$$

Here, τ refers to the shear strength of the matrix. Overall, the energy from the deformation of the thermoplastic composite is $E_S = \frac{\cos\alpha}{\cos(\phi-\alpha)\cdot\sin\phi} \cdot \tau$.

For different FOAs, the cutting mechanism may vary and in turn the total energy for each FOA may differ. In addition to the energy released from the plastic deformation of the PP matrix due to the combined shear and tensile forces, the following components may contribute to the fracture energy under different FOAs.

For the cutting condition when FOA = 0 deg, the cutting mechanism is related mainly to matrix deforming and very little fiber–matrix debonding and/or interfacial shearing of fibers. The matrix shear debonding energy is denoted by W_S, with the propagating failure at distance L, given by [59]:

$$W_S = 2\pi r_0 \tau_0 L/\gamma \tag{9}$$

Here, r_0 is the fiber radius, τ_0 is the maximum boundary shear stress at the fracture, and the stress concentration coefficient $\gamma = (2G/E)^{1/2}/r_0 \cdot \ln(r_1/r_0)$, where $r_1 - r_0$ is the matrix thickness, G is the matrix shear modulus, and E is the elastic modulus of the fiber.

Based on a square packing geometry assumption, the fracture energy per unit area A of such a condition can be rewritten as [59] follows:

$$\frac{W^{(0)}}{A} = \frac{W_S^{(0)}}{A} = \tau_0 \left(\frac{E}{2G}\right)^{\frac{1}{2}} L_h f_1(V) f_2(V) \tag{10}$$

In contrast, for FOA = 90 deg (shown in Fig. 13(*b*)), the flax fibers in the workpiece undergo stresses along the fiber–matrix boundaries in the primary shear zone. Hence, the energy released during orthogonal cutting consists of (1) the matrix material deformation in the shear zone, (2) fiber failure (breakage and pull-out from the matrix), (3) interfacial friction between fiber–matrix bonds, (4) chip motion and material entanglement on the rake face, and (5) the interaction between clearance face of the tool and the machined surface. Here we only consider the AE energy released from the sources 1–3. This is because these are considered as primary sources of AE during NFRP machining, and they can be physically related to the underlying microdynamics, especially the material removal mechanisms prevailing under different fiber orientations.

The summation of the friction energy [59] between the fiber and the matrix boundary with a constant friction force, $\tau_f = (f/\pi d)dx$, between the fibers and the boundary of the matrix in the effective region/length of l is as follows:

$$P_f = \pi d \tau_f l \tag{11}$$

When a debonded fiber separates off over length $l = L_f$ inside the matrix, the friction work W_f between the fiber and the matrix can be formulated as follows:

$$W_f = -\int_{l=L_f}^{l=0} 2\pi r_0 \tau_f dl = \pi r_0 \tau_f L_f^2 \tag{12}$$

Table 4 Physical properties of the NFRPs materials

List of physical properties	
Fiber radius r_0	~10 μm
Fiber tensile strength σ_0	~500 MPa [54,55]
PP matrix tensile strength	~29.5 MPa [55,56]
Maximal shear stress debonding	~2 MPa [57]
Fiber Young modulus E	~50 GPa [55]
PP matrix Young modulus E	~1 GPa
Constant frictional stress τ_f	7–40 MPa
Possible range of shearing stress	30 MPa [58]
Fiber volume fracture V	0.4
Fiber packing	Square (4 nearest neighborhoods)
Volume fraction functions	$f_1(V) \approx 0.7676$, $f_2(V) = 0.4$, and $f_3(V) = 0.3568$

The fracture energy for the fiber breakage/ pull-out is represented [59] as follows:

$$W_D = \frac{\pi r_o^2}{2E} \int_{l=0}^{l=L_D} \left(\sigma - \frac{2\tau_f l}{r} \right)^2 dl \tag{13}$$

By substituting $L = r_0\sigma/2\tau_f$, we have

$$W_D = \frac{\pi r_o^2 \sigma^2 L}{6E} \tag{14}$$

Considering the cutting speed and the square packing geometry assumption, in addition to the energy released from the matrix deformation, the fracture energy under FOA = 90 deg contains the following: (1) the energy released from fiber tensile failure per unit area A, $W_D/A = (\sigma_0^2/12E)\, L_b f_2(V)$ and (2) the energy released from friction per unit area A, $W_f/A = (\tau_f L_f/2r_0) f_2(V)$. Here, the maximum debonding length $L_b = r_0$ and the volume fraction functions are $f_1(V) = \ln(r_1/r_0) = \{\ln[(\pi/V)^{1/2} - 1\ ]\}^{1/2}$, $f_2(V) = V$, and $f_3(V) = (V/\pi)^{1/2}$ [60]. The maximum debonding length is $L_b = (r_0/\tau_f)[(\sigma_b/2) - \tau_0(E/2G)^{1/2} f_1(V)]$, and we assume that $L_f \approx L_b$. Note that Table 4 lists the values of all physical properties related to energy released under different types of failure modes. Hence, as the cutting speed v increases and more area A is machined per unit time ($A = b \cdot v$, where b is the width of the chip and is approximately equivalent to the width of the sample for all experiments). Consequently, more fracture energy is released at higher cutting speeds, resulting in significantly different AE envelopes under different cutting speeds as suggested in Fig. 10.

Relative to connecting the AE responses to various failure modes, earlier efforts [23,51,61] included extensive mechanical tests on the composite materials and applied frequency analysis to the resulting acoustic emission signals for different types of failures. A summary of the frequency responses of AE signals to different failure mechanisms of fiber-reinforced composites is listed in Table 5. Matching significant frequency features (results from random forest classifications with the highest Gini coefficients) with the AE characteristics (frequency responses) for different failures modes allows us to identify different failure modes related to the prevalent cutting mechanisms under distinct fiber orientations.

As shown in Figs. 11(*a*), 11(*b*), and 11(*d*), the AE frequency responses ranging from 350 kHz to 440 kHz distinguish FOA = 0 deg from other angles. That is, compared with the fiber debonding (which has an AE frequency response in the range from 240 kHz to 310 kHz), which is prevalent under orthogonal cutting with 0 deg FOA, the frequency responses related to fiber breakage (350 kHz to 440 kHz) are more significant for both FOA = 45 deg and 90 deg. When we compare the results of FOA = 45 deg versus 90 deg, even though differences in frequency components are less noticeable as shown in Fig. 11(*f*), the random forest approach is capable of picking up most significant frequency features (within frequency ranges of 260 kHz–280 Hz and 220–240 kHz) to achieve a classification accuracy around 95.3%. Table 5 suggests that these frequency features determining the classification accuracy for FOA = 45 deg versus 90 deg are related to fiber–matrix debonding and fiber pull-out [23], which are fundamental cutting mechanisms that distinguish the machining processes between FOA = 45 deg and 90 deg [53]. As for the 45-deg orientation position, the cutting mechanism consists of compression induced interfacial shearing along the fiber orientation direction that causes fiber–matrix debonding; for FOA = 90 deg, the fractures that contribute predominantly to fiber pull-out emerge intermittently (this may be one reason that the AE waveform under 90 deg shows a significant transient pattern compared with the others). Moreover, fiber breakage is prevalent for both FOA = 45 deg and 90 deg cases. This prevalence may be one reason that the AE frequency responses (350 kHz–440 kHz) to the fiber breakage are less significant in discerning the changes between cutting mechanisms under FOA = 45 deg and 90 deg conditions.

Table 5 Dominant range of frequency response (kHz) to fracture energy [61–63]

Failure mode	Frequency response (kHz)
Matrix failure	90–180
Fiber–matrix debonding	240–310
Fiber breakage	>350

5 Conclusions

This paper presented the framework of an in-process monitoring scheme for machining processes of NFRP materials. By using a random forest model, we showed that AE signals contain relevant information pertaining to the process. The main contributions of this paper are as follows:

- An in-process monitoring scheme with a multiple-sensor setup for gathering vibrations as well as the acoustic emission information during orthogonal cutting of the NFRP has been discussed. Different machining conditions and material removal routes were analyzed using the AE signals, namely, (a) cutting versus no cutting and (b) cutting with different fiber orientations.
- A random forest algorithm was applied for supervised monitoring of the processes with accuracy around 95% to distinguish various fiber orientations toward the cutting direction that are related to distinct cutting mechanisms. Results from the random forest approach indicate that the high-frequency information from the captured acoustic emission signals reflects fundamental cutting mechanism changes.
- Further analysis shows that the most significant frequency responses determining the accuracy of the random forest model are highly related to the distinct failure modes under various fiber orientation conditions. Hence, the presented

approach connects the AE characteristics to the microdynamics of machining NFRPs.

We note that AE features considered in the present work aggregates multiple mechanisms prevalent during the machining of NFRP composites. Process conditions, especially the cutting speed, determine the material deformation rate. Since AE is released from the various material deformation and fracture mechanisms during NFRP machining, the time and frequency characteristics of the AE waveform varies with the cutting speed. The cutting speed also affects the dynamics of fiber deformation and fracture, matrix failure, as well as the actions at the primary and the secondary and tertiary deformation zones. Particularly, this variation in the AE waveform characteristics in the 50–100 kHz band (as noted by the Gini index) can be used to identify the process condition, including the cutting speed and FOA. The AE waveform, as gathered, is a composition of elementary AE pulses released from various different sources. Toward using the results of these predictions for process control, it would be desirable to isolate contributions of individual source in the measured AE signal. Also, for future work, other factors, such as the effect of fiber (bundle) distributions and chip formations, need to be considered for further AE analysis. Further advances in the analytical approach is needed for identifying how various transient components from specific sources are composed in the measured AE signals to diagnose incipient anomalies during the machining of NFRPs. We also note that the present approach can be applied for predicting process conditions during machining of different types of composite materials. Further experimental studies within machining of alternative composites materials (e.g., synthetic fiber-reinforced plastics or biocomposites) are needed to identify the chief material removal and surface modification mechanism, characterize the resulting AE waveforms, as well as to develop practical methods to monitor in machining process performance and surface quality in real time.

Acknowledgment

The authors thank the National Science Foundation (CMMI #1432914) for supporting the research.

References

[1] Chegdani, F., Takabi, B., Tai, B. L., El Mansori, M., and Bukkapatnam, S. T., 2018, "Thermal Effects on Tribological Behavior in Machining Natural Fiber Composites," Proc. Manuf., **26**, pp. 305–316.
[2] Chegdani, F., Wang, Z., El Mansori, M., and Bukkapatnam, S. T., 2018, "Multiscale Tribo-Mechanical Analysis of Natural Fiber Composites for Manufacturing Applications," Tribol. Int., **122**, pp. 143–150.
[3] Holbery, J., and Houston, D., 2006, "Natural-Fiber-Reinforced Polymer Composites in Automotive Applications," JOM, **58**(11), pp. 80–86.
[4] Al-Oqla, F. M., and Sapuan, S., 2014, "Natural Fiber Reinforced Polymer Composites in Industrial Applications: Feasibility of Date Palm Fibers for Sustainable Automotive Industry," ASME J. Cleaner Prod., **66**, pp. 347–354.
[5] Ramulu, M., 1997, "Machining and Surface Integrity of Fibre-Reinforced Plastic Composites," Sadhana, **22**(3), pp. 449–472.
[6] Herrera-Franco, P., and Valadez-Gonzalez, A., 2005, "A Study of the Mechanical Properties of Short Natural-Fiber Reinforced Composites," Compos. Part B Eng., **36**(8), pp. 597–608.
[7] Ku, H., Wang, H., Pattarachaiyakoop, N., and Trada, M., 2011, "A Review on the Tensile Properties of Natural Fiber Reinforced Polymer Composites," Compos. Part B Eng., **42**(4), pp. 856–873.
[8] Nassar, M. M., Arunachalam, R., and Alzebdeh, K. I., 2017, "Machinability of Natural Fiber Reinforced Composites: A Review," Int. J. Adv. Manuf. Technol., **88**(9–12), pp. 2985–3004.
[9] Chegdani, F., and El Mansori, M., 2018, "Mechanics of Material Removal When Cutting Natural Fiber Reinforced Thermoplastic Composites," Polym. Test., **67**, pp. 275–283.
[10] De Rosa, I. M., Santulli, C., and Sarasini, F., 2009, "Acoustic Emission for Monitoring the Mechanical Behaviour of Natural Fibre Composites: A Literature Review," Compos. Part A: Appl. Sci. Manuf., **40**(9), pp. 1456–1469.
[11] Herrera-Franco, P., and Valadez-Gonzalez, A., 2004, "Mechanical Properties of Continuous Natural Fibre-Reinforced Polymer Composites," Compos. Part A: Appl. Sci. Manuf., **35**(3), pp. 339–345.
[12] Romhány, G., Karger-Kocsis, J., and Czigány, T., 2003, "Tensile Fracture and Failure Behavior of Thermoplastic Starch With Unidirectional and Cross-ply Flax Fiber Reinforcements," Macromol. Mater. Eng., **288**(9), pp. 699–707.
[13] Babu, G. D., Babu, K. S., and Gowd, B. U. M., 2013, "Effect of Machining Parameters on Milled Natural Fiber-Reinforced Plastic Composites," ASME J. Adv. Mech. Eng., **1**, pp. 1–12.
[14] George, J., Sreekala, M., and Thomas, S., 2001, "A Review on Interface Modification and Characterization of Natural Fiber Reinforced Plastic Composites," Polym. Eng. Sci., **41**(9), pp. 1471–1485.
[15] Valadez-Gonzalez, A., Cervantes-Uc, J. M., Olayo, R., and Herrera-Franco, P. J., 1999, "Effect of Fiber Surface Treatment on the Fiber–Matrix Bond Strength of Natural Fiber Reinforced Composites," Compos. Part B: Eng., **30**(3), pp. 309–320.
[16] Teti, R., Jemielniak, K., O'Donnell, G., and Dornfeld, D., 2010, "Advanced Monitoring of Machining Operations," CIRP Ann. Manuf. Technol., **59**(2), pp. 717–739.
[17] Chegdani, F., Mezghani, S., El Mansori, M., and Mkaddem, A., 2015, "Fiber Type Effect on Tribological Behavior When Cutting Natural Fiber Reinforced Plastics," Wear, **332**, pp. 772–779.
[18] Lee, D.-E., Hwang, I., Valente, C. M., Oliveira, J., and Dornfeld, D. A., 2006, "Precision Manufacturing Process Monitoring With Acoustic Emission," Int. J. Mach. Tools Manuf., **46**(2), pp. 176–188.
[19] Uehara, K., and Kanda, Y., 1984, "Identification of Chip Formation Mechanism Through Acoustic Emission Measurements," CIRP Ann. Manuf. Technol., **33**(1), pp. 71–74.
[20] Bhuiyan, M., Choudhury, I., and Nukman, Y., 2012, "An Innovative Approach to Monitor the Chip Formation Effect on Tool State Using Acoustic Emission in Turning," Int. J. Mach. Tools Manuf., **58**, pp. 19–28.
[21] Margueres, P., Meraghni, F., and Benzeggagh, M., 2000, "Comparison of Stiffness Measurements and Damage Investigation Techniques for a Fatigued and Post-Impact Fatigued GFRP Composite Obtained by RTM Process," Compos. Part A: Appl. Sci. Manuf., **31**(2), pp. 151–163.
[22] Davidovitz, M., Mittelman, A., Roman, I., and Marom, G., 1984, "Failure Modes and Fracture Mechanisms in Flexure of Kevlar-Epoxy Composites," ASME J. Mater. Sci., **19**(2), pp. 377–384.
[23] Mizutani, Y., Nagashima, K., Takemoto, M., and Ono, K., 2000, "Fracture Mechanism Characterization of Cross-ply Carbon-Fiber Composites Using Acoustic Emission Analysis," NDT E Int., **33**(2), pp. 101–110.
[24] Dornfeld, D., and Kannatey-Asibu, E., 1980, "Acoustic Emission During Orthogonal Metal Cutting," Int. J. Mech. Sci., **22**(5), pp. 285–296.
[25] Kannatey-Asibu, E., and Dornfeld, D. A., 1981, "Quantitative Relationships for Acoustic Emission From Orthogonal Metal Cutting," ASME J. Eng. Ind., **103**(3), pp. 330–340.
[26] Kamarthi, S. V., Kumara, S. R., and Cohen, P. H., 1995, "Wavelet Representation of Acoustic Emission in Turning Process," Proceedings of the 1995 Artificial Neural Networks in Engineering, ANNIE'95, St. Louis, MO, Nov. 12–15.
[27] Pittner, S., Kamarthi, S. V., and Gao, Q., 1998, "Wavelet Networks for Sensor Signal Classification in Flank Wear Assessment," ASME J. Intell. Manuf., **9**(4), pp. 315–322.
[28] Pittner, S., and Kamarthi, S. V., 1999, "Feature Extraction From Wavelet Coefficients for Pattern Recognition Tasks," IEEE Trans. Pattern Anal. Machine Intell., **21**(1), pp. 83–88.
[29] Bukkapatnam, S. T., Kumara, S. R., and Lakhtakia, A., 2000, "Fractal Estimation of Flank Wear in Turning," ASME J. Dyn. Syst. Meas. Control, **122**(1), pp. 89–94.
[30] Rao, P., Bukkapatnam, S., Beyca, O., Kong, Z. J., and Komanduri, R., 2014, "Real-Time Identification of Incipient Surface Morphology Variations in Ultraprecision Machining Process," ASME J. Manuf. Sci. Eng., **136**(2), p. 021008.
[31] Cheng, C., Wang, Z., Hung, W., Bukkapatnam, S. T., and Komanduri, R., 2015, "Ultra-Precision Machining Process Dynamics and Surface Quality Monitoring," Proc. Manuf., **1**, pp. 607–618.
[32] Kannatey-Asibu, E., Jr., and Dornfeld, D., 1982, "A Study of Tool Wear Using Statistical Analysis of Metal-Cutting Acoustic Emission," Wear, **76**(2), pp. 247–261.
[33] Wang, Z., and Bukkapatnam, S. T., 2018, "A Dirichlet Process Gaussian State Machine Model for Change Detection in Transient Processes," Technometrics, **60**(3), pp. 1–13.
[34] Chang, D.-C., and Bukkapatnam, S., 2004, "Towards Characterizing the Microdynamics of AE Generation in Machining," Machining Sci. Technol., **8**(2), pp. 235–261.
[35] Bukkapatnam, S., and Chang, D.-C., 2005, "A Statistical Mechanistic Model of Acoustic Emission Generation in Shear Zone of Machining," Trans. NAMRI/SME, **33**, pp. 597–604.
[36] Arul, S., Vijayaraghavan, L., and Malhotra, S., 2007, "Online Monitoring of Acoustic Emission for Quality Control in Drilling of Polymeric Composites," ASME J. Mater. Process. Technol., **185**(1–3), pp. 184–190.
[37] Velayudham, A., Krishnamurthy, R., and Soundarapandian, T., 2005, "Acoustic Emission Based Drill Condition Monitoring During Drilling of Glass/Phenolic Polymeric Composite Using Wavelet Packet Transform," Mater. Sci. Eng. A, **412**(1), pp. 141–145.
[38] Hase, A., Wada, M., Koga, T., and Mishina, H., 2014, "The Relationship Between Acoustic Emission Signals and Cutting Phenomena in Turning Process," Int. J. Adv. Manuf. Technol., **70**(5–8), pp. 947–955.
[39] Menze, B. H., Kelm, B. M., Masuch, R., Himmelreich, U., Bachert, P., Petrich, W., and Hamprecht, F. A., 2009, "A Comparison of Random Forest and Its Gini Importance With Standard Chemometric Methods for the Feature Selection and Classification of Spectral Data," BMC Bioinf., **10**(1), p. 213.

[40] Bukkapatnam, S. T., Kumara, S. R., and Lakhtakia, A., 1999, "Local Eigenfunctions Based Suboptimal Wavelet Packet Representation of Contaminated Chaotic Signals," IMA J. Appl. Mathematics, **63**(2), pp. 149–162.
[41] Bukkapatnam, S. T., Kumara, S. R., and Lakhtakia, A., 1999, "Analysis of Acoustic Emission Signals in Machining," ASME J. Manuf. Sci. Eng., **121**(4), pp. 568–576.
[42] Iquebal, A. S., Bukkapatnam, S., and Srinivasa, A., 2017, "Change Detection in Complex Dynamical Systems Using Intrinsic Phase and Amplitude Synchronization," preprint arXiv:1701.00610.
[43] Liaw, A., and Wiener, M., 2002, "Classification and Regression by RandomForest," R News, **2**(3), pp. 18–22.
[44] Botcha, B., Rajagopal, V., Babu N, R., and Bukkapatnam, S. T. S., 2018, "Process-Machine Interactions and a Multi-Sensor Fusion Approach to Predict Surface Roughness in Cylindrical Plunge Grinding Process," Proc. Manuf., **26**, pp. 700–711.
[45] Arumugam, J., Bukkapatnam, S. T., Narayanan, K. R., and Srinivasa, A. R., 2016, "Random Forests Are Able to Identify Differences in Clotting Dynamics From Kinetic Models of Thrombin Generation," PLoS One, **11**(5), p. e0153776.
[46] Afrin, K., Illangovan, G., Srivatsa, S. S., and Bukkapatnam, S. T., 2018, "Balanced Random Survival Forests for Extremely Unbalanced, Right Censored Data," preprint arXiv:1803.09177.
[47] Wu, D., Jennings, C., Terpenny, J., Gao, R. X., and Kumara, S., 2017, "A Comparative Study on Machine Learning Algorithms for Smart Manufacturing: Tool Wear Prediction Using Random Forests," ASME J. Manuf. Sci. Eng., **139**(7), p. 071018.
[48] Wambua, P., Ivens, J., and Verpoest, I., 2003, "Natural Fibres: Can They Replace Glass in Fibre Reinforced Plastics?," Compos. Sci. Technol., **63**(9), pp. 1259–1264.
[49] Mahdi, M., and Zhang, L., 2001, "A Finite Element Model for the Orthogonal Cutting of Fiber-Reinforced Composite Materials," J. Mater. Process. Technol., **113**(1–3), pp. 373–377.
[50] Eriksen, E., 1999, "Influence From Production Parameters on the Surface Roughness of a Machined Short Fibre Reinforced Thermoplastic," Int. J. Mach. Tools Manuf., **39**(10), pp. 1611–1618.
[51] Nazmdar Shahri, M., Yousefi, J., Fotouhi, M., and Ahmadi Najfabadi, M., 2016, "Damage Evaluation of Composite Materials Using Acoustic Emission Features and Hilbert Transform," J. Compos. Mater., **50**(14), pp. 1897–1907.
[52] Park, J.-M., Son, T. Q., Jung, J.-G., and Hwang, B.-S., 2006, "Interfacial Evaluation of Single Ramie and Kenaf Fiber/Epoxy Resin Composites Using Micromechanical Test and Nondestructive Acoustic Emission," Compos. Interfaces, **13**(2–3), pp. 105–129.
[53] Ramulu, M., Kim, D., and Choi, G., 2003, "Frequency Analysis and Characterization in Orthogonal Cutting of Glass Fiber Reinforced Composites," Compos. Part A: Appl. Sci. Manuf., **34**(10), pp. 949–962.
[54] Alves Fidelis, M. E., Pereira, T. V. C., Gomes, O. d. F. M., de Andrade Silva, F., and Toledo Filho, R. D., 2013, "The Effect of Fiber Morphology on the Tensile Strength of Natural Fibers," J. Mater. Res. Technol., **2**(2), pp. 149–157.
[55] Chegdani, F., Mezghani, S., and El Mansori, M., 2015, "Experimental Study of Coated Tools Effects in Dry Cutting of Natural Fiber Reinforced Plastics," Surf. Coat. Technol., **284**, pp. 264–272.
[56] Shubhra, Q. T., Alam, A., and Quaiyyum, M., 2013, "Mechanical Properties of Polypropylene Composites: A Review," J. Thermoplast. Compos. Mater., **26**(3), pp. 362–391.
[57] Khalil, H. P. S. A., Ismail, H., Rozman, H. D., and Ahmad, M. N., 2001, "The Effect of Acetylation on Interfacial Shear Strength Between Plant Fibres and Various Matrices," Eur. Polym. J., **37**(5), pp. 1037–1045.
[58] Hsueh, C.-H., 1990, "Interfacial Debonding and Fiber Pull-Out Stresses of Fiber-Reinforced Composites," Mater. Sci. Eng. A, **123**(1), pp. 1–11.
[59] Kaelble, D., 1973, "Theory and Analysis of Fracture Energy in Fiber Reinforced Composites," J. Adhes., **5**(3), pp. 245–264.
[60] Wells, J., and Beaumont, P., 1985, "Debonding and Pull-Out Processes in Fibrous Composites," J. Mater. Sci., **20**(4), pp. 1275–1284.
[61] Nimdum, P., and Renard, J., 2012, "Use of Acoustic Emission to Discriminate Damage Modes in Carbon Fibre Reinforced Epoxy Laminate During Tensile and Buckling Loading," ECCM 15-15th European Conference on Composite Materials, Venice, Italy, June 24–28.
[62] de Groot, P. J., Wijnen, P. A. M., and Janssen, R. B. F., 1995, "Real-Time Frequency Determination of Acoustic Emission for Different Fracture Mechanisms in Carbon/Epoxy Composites," Compos. Sci. Technol., **55**(4), pp. 405–412.
[63] Park, J.-M., Kim, P.-G., Jang, J.-H., Wang, Z., Hwang, B.-S., and DeVries, K. L., 2008, "Interfacial Evaluation and Durability of Modified Jute Fibers/Polypropylene (PP) Composites Using Micromechanical Test and Acoustic Emission," Compos. Part B: Eng., **39**(6), pp. 1042–1061.